



Ballistic penetration of deforming metallic plates: Experimental and numerical investigation

Lang Li^{a,b,c,*}, Qian-Cheng Zhang^c, Tian Jian Lu^{b,d}

^a School of Mechanics, Civil Engineering and Architecture, Northwestern Polytechnical University, Xi'an 710072, P.R. China

^b State Key Laboratory of Mechanics and Control of Mechanical Structures, Nanjing University of Aeronautics and Astronautics, Nanjing 210016, P.R. China

^c State Key Laboratory for Strength and Vibration of Mechanical Structures, Xi'an Jiaotong University, Xi'an 710049, P.R. China

^d MITT Key Laboratory of Multifunctional Lightweight Materials and Structures, Nanjing University of Aeronautics and Astronautics, Nanjing 210016, P.R. China

ARTICLE INFO

Keywords:

Ballistic penetration
Deforming steel plate
Experiment
Numerical simulation
Anti-penetration design

ABSTRACT

A combined experimental and numerical investigation is carried out to study systematically the ballistic performance of a metallic plate that deforms continuously under pre-imparted impulsive loading (e.g., due to TNT explosion) before being impacted by a projectile. First, based on a novel experimental method, ballistic impact test of a deforming thin steel plate is performed via a one-stage gas gun; as benchmark, ballistic impact test of a static (non-deforming) thin steel plate via a two-stage gas gun is also performed. Results show that deforming has significant influence on ballistic performance of metallic plates in terms of perforation mode and ballistic limit. Then, based on three-dimensional finite element simulations that are validated against experimental measurements, physical mechanisms underlying the deforming effect are explored. The effects of pre-imparted impulse, the shock resistance of target plate, and the nose shape of projectile on the ballistic performance are also quantified. It is demonstrated that deforming leads to changes of the projectile-target system in three aspects: providing initial kinetic energy to target, changing plastic deformation in dished region, and altering shear force during perforation. The interaction of these three aspects dictates the ballistic performance of a deforming target plate. The results are employed to carry out anti-penetration design for deforming steel plates.

1. Introduction

Steel plates are widely used to construct civilian and military sub-structures, such as hulls of ships, fuselages, and chassis of cars. While the main focus was placed upon load carrying capacity in early times, their ballistic resistance performance received increasing attention later on [1–4]. Generally, the target plates are in static state, e.g., ballistic penetration of a static thin steel plate. In some cases, however, the target plates suffer combined blast and fragment impact loading, generated say by cased-explosives such as roadside bombings and improvised explosive devices (IEDs) [5–7]. As the velocity of blast wave propagation is different from that of fragment flying, there exists one situation that, while a target plate is deformed by blast loading, it is also penetrated by fragments simultaneously, namely, ballistic impact on a deforming target plate.

The ballistic penetration behaviors of a wide variety of metallic plates have been extensively investigated using experimental, analytical and numerical methods [8–27]. The focus has primarily been placed

upon how different factors influence the ballistic resistance of the target plate and the underlying penetration mechanics. Key factors that have been considered include those associated with the projectiles such as nose shape [8–11] and hardness [12–13], those with the targets such as monolithic or layered (either in-contact or separated) [14–18], strength and ductility [19], strain rate sensitivity and strain hardening [20], thickness [21–23], and those with the loading conditions such as impact velocity and incidence angle [24,25]. However, existing studies mainly considered static metallic plates, and few reported on ballistic penetration of deforming thin steel plates, in spite that this is a pretty common situation when cased-explosives are considered. Chen et al. [26–27] investigated the effect of a soft nose on the penetration of metallic plates: the soft nose initiated an ahead structural response (deforming) of the plate, which was found to have notable influence on penetration. It is therefore of importance to investigate systematically the ballistic performance of deforming metallic plates.

For a deforming metallic plate subjected to projectile penetration, experimental tests provide a primary cognition while numerical

* Corresponding author at: Northwestern Polytechnical University, Xi'an 710072, P.R. China

E-mail addresses: lilang@nwpu.edu.cn (L. Li), zqc111999@xjtu.edu.cn (Q.-C. Zhang), tjlu@nuaa.edu.cn (T.J. Lu).

<https://doi.org/10.1016/j.ijimpeng.2022.104359>

Received 7 April 2022; Received in revised form 6 August 2022; Accepted 15 August 2022

Available online 17 August 2022

0734-743X/© 2022 Elsevier Ltd. All rights reserved.

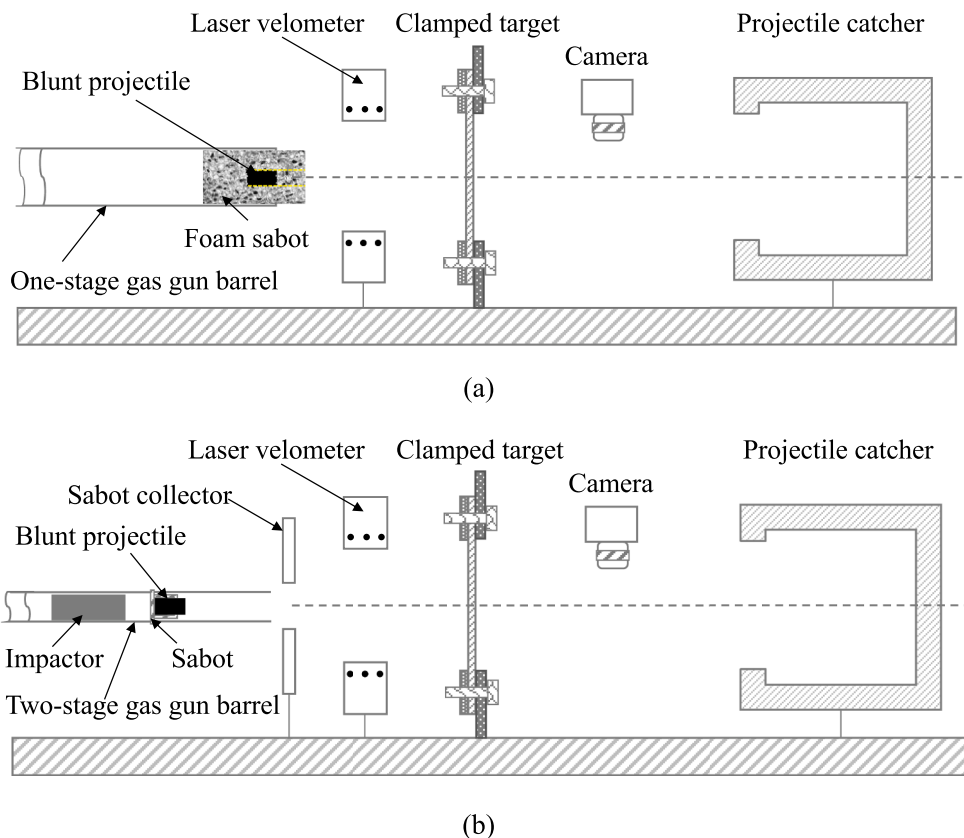


Fig. 1. Schematic of impact experimental setup: (a) one-stage gas gun; (b) two-stage gas gun.

simulations provide a choice to reveal the underlying mechanisms. However, at present, the ballistic impact test of a deforming metallic plate is yet performed experimentally. At the laboratory scale, light-gas gun is the most common choice for impact tests, due to its safety, stability and economy. Through sudden release of compressed gas, the projectile loaded into the gas gun barrel is accelerated to strike the target. Traditionally, when a solid projectile is loaded, the technique can be used to perform ballistic impact tests on static targets [28–29]; when an aluminum (Al) foam projectile is loaded, the technique can be used to perform simulate shock tests on static targets [30–31]. More recently, the present authors proposed to embed a projectile into a Al foam sabot to construct a novel composite projectile which, when loaded into the light-gas gun, enables performing combined shock and projectile impact tests on static targets [32]. For a composite projectile with purposely

selected impact velocity, the Al foam sabot arrives at the target first to generate a shock loading that forces the originally static target to deflect (deform); subsequently, while the target continues to deform, the embedded projectile arrives and starts to penetrate the deforming target. Therefore, the proposed composite projectile is deemed suitable for conducting ballistic impact test on a deforming target. In contrast, the composite projectile can also be designed to enable the projectile striking the static target first, followed by the impact of Al foam projectile.

With the light-gas gun setup, most numerical simulations on target plates impacted by Al foam projectiles only tracked the macroscopic properties of the foam [31–32]. However, it has been demonstrated that the dynamic deformation of a cellular foam may be affected by micro-inertia [33]. As the shock loading generated by a Al foam

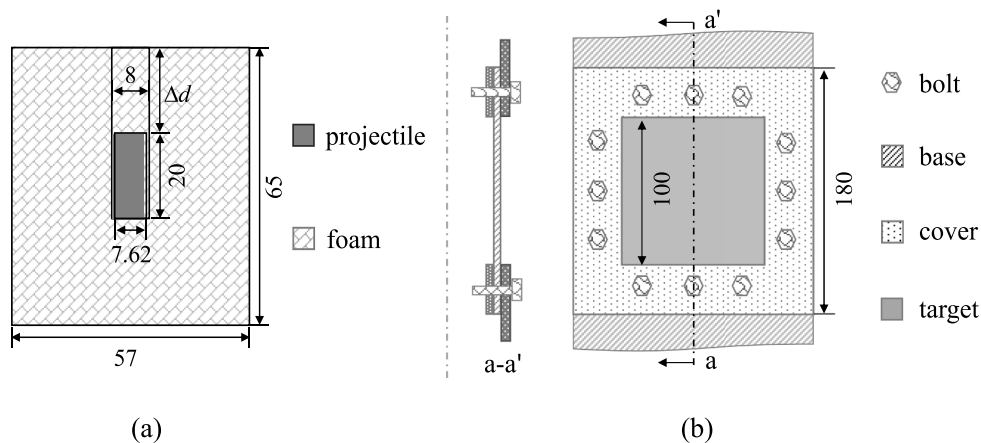


Fig. 2. Schematic of (a) blunt projectile with foam sabot and (b) target plate and boundary setting (measured in mm).

Table 1

Loading conditions and results of the tests (mass of the foam sabot m_f , mass of the blunt projectile m_b , initial projectile velocity v_i and residual projectile velocity v_r).

Tests	Specimen types	Δd (mm)	m_f (g)	m_b (g)	v_i (m/s)	v_r (m/s)
#1-1	Static	–	–	7.1	125	0
#1-2	Static	–	–	7.1	152	80
#1-3	Static	–	–	7.1	177	117
#1-4	Static	–	–	7.1	244	205
#1-5	Static	–	–	7.1	292	267
#1-6	Static	–	–	7.1	310	283
#1-7	Static	–	–	7.1	320	298
#1-8	Static	–	–	7.1	348	323
#2-1	Deforming	15	61.7	7.1	105	0
#2-2	Deforming	15	60.3	7.1	149	105
#2-3	Deforming	15	62.5	7.1	185	152
#2-4	Deforming	15	61.9	7.1	236	208
#2-5	Deforming	15	62.3	7.1	299	269
#2-6	Deforming	15	61.2	7.1	336	307
#3-1	Deforming	5	59.8	7.1	136	0
#3-2	Deforming	5	61.3	7.1	159	86
#3-3	Deforming	5	60.7	7.1	199	133
#3-4	Deforming	5	62.2	7.1	249	196
#3-5	Deforming	5	60.3	7.1	275	225
#3-6	Deforming	5	61.5	7.1	320	282

projectile is highly dependent upon its dynamic deformation, using a full foam model with three-dimensional (3D) cellular structure to simulate the factual foam projectile becomes a necessity. Two different types of 3D mesoscopic foam model have been commonly used to represent a real cellular foam, i.e., the 3D foam structure reconstructed by using the technique of X-Ray computer tomography [34,35] and the 3D Voronoi structure constructed by dividing a 3D space [36,37]. Compared with the solid elements in X-Ray reconstructed model, the 3D Voronoi foam model is meshed by shell elements, thus exhibiting higher efficiency for numerical calculation.

The current study aims to characterize the ballistic resistance performance of deforming steel plates and explore physical mechanisms underlying the deforming effect by using a combined experimental and numerical approach. The paper is organized as follows. In Section 2, a series of ballistic impact tests for both static and deforming steel plates are conducted and the results are presented in terms of failure modes of target plate and residual velocity of projectile. Finite element (FE) models on cell-based foam sabot and solid projectile is constructed in Section 3. In Section 4, upon validating the proposed FE models against experimental measurements, the underlying mechanisms involved in the ballistic penetration of a deforming target are quantitatively analyzed via FE simulations. The effects of pre-imparted impulse, shock resistance of target plate, and nose shape of projectile on ballistic resistance are explored. In Section 5, for practical applications, anti-penetration design of deforming thin steel plates is illustrated.

2. Experimental investigation

2.1. Experimental set-up

Ballistic impact tests for deforming thin steel plates were carried out by using an one-stage gas gun (bore diameter 57 mm), as shown in Fig. 1a. In the test, a blunt projectile with aluminum foam sabot (Fig. 2a) was accelerated and projected on the thin steel plate. For reference, ballistic impact tests for static thin steel plates subjected to blunt projectile were also performed based on a two-stage gas gun, as shown in Fig. 1b. A high-speed video camera (I-SPEED 716, IX) was used to record the residual velocity of the projectile perforating the target, while its incident velocity was measured by laser velocimeter.

The blunt cylindrical projectiles employed in both impact tests were made of hardened steel, thus could be considered as rigid during ballistic penetration. The size of each blunt projectile was 20 mm in length and

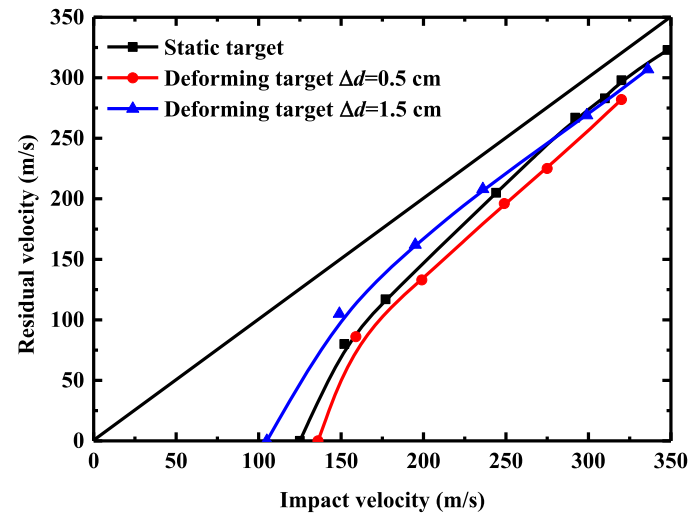


Fig. 3. Residual velocity of blunt projectile plotted as a function of impact velocity: comparison between static and deforming steel plates for $\Delta d = 0.5$ cm and $\Delta d = 1.5$ cm.

7.62 mm in diameter, whose mass is nearly 7.1 g for all tests; Fig. 2a. The cylindrical aluminum foam sabot was 65 mm in length and 57 mm in diameter, while its cylindrical inner hole had a diameter of 8 mm, slightly larger than that of the projectile. The cylindrical foam sabot was electro-discharge machined from a block of closed-cell aluminum foam which had a relative density of 13.7% and a compressive plateau strength of approximately 4.5 MPa. Since the distribution and morphology of the core in the aluminum foam block was irregularly, the mass of each foam sabot taken from the foam block was different, detailed values of the masses are presented in Table 1. The length of inner hole was larger than the length of blunt projectile that it housed, leaving a depth Δd between the front surface of foam sabot and the top of projectile; Fig. 2a. In the present study, two values of hole depth were selected, i.e., $\Delta d = 0.5$ cm and $\Delta d = 1.5$ cm, to study the ballistic performance of deforming thin steel plates.

Square Q235 steel plates (180 mm in width and 0.9 mm in thickness) were fully clamped and fastened along each edge by a cover strip (40 mm in width) and a base frame, leaving an exposed area of 100 mm \times 100 mm; Fig. 2b. The yield strength and strain hardening slope of Q235 steel are 293 MPa and 600 MPa, respectively.

2.2. Measurements and observations

The experimental program and some test results of the three groups of shots were given in Table 1, while the ballistic performance of deforming steel plates was compared with that of static ones in terms of residual projectile velocity in Fig. 3. The residual velocity of the projectile after penetrating a static target was found to be larger than its counterpart after penetrating a deforming target when $\Delta d = 0.5$ cm for all impact velocities tested, but lower than the latter when $\Delta d = 1.5$ cm for impact velocities lower than 275 m/s. These results indicated that significant influence of deforming on ballistic performance. Besides, comparison between deforming targets impacted by projectiles embedded in foam sabots having different Δd showed that the penetration resistance was also strongly affected by the deforming extent of target, which varied as Δd was changed. It should be noted that the corresponding impact velocities whose residual velocities were zero were not the ballistic limit velocities, but situations not giving perforation. Due to the limitations of the employed gas gun, the ballistic limit velocities are not obtained experimentally. The ballistic limit velocities employed in the following discussion would be calculated numerically.

Fig. 4 presented cross-sectional views of perforated thin steel plates, with the test impact velocity marked in the lower-right corner of each

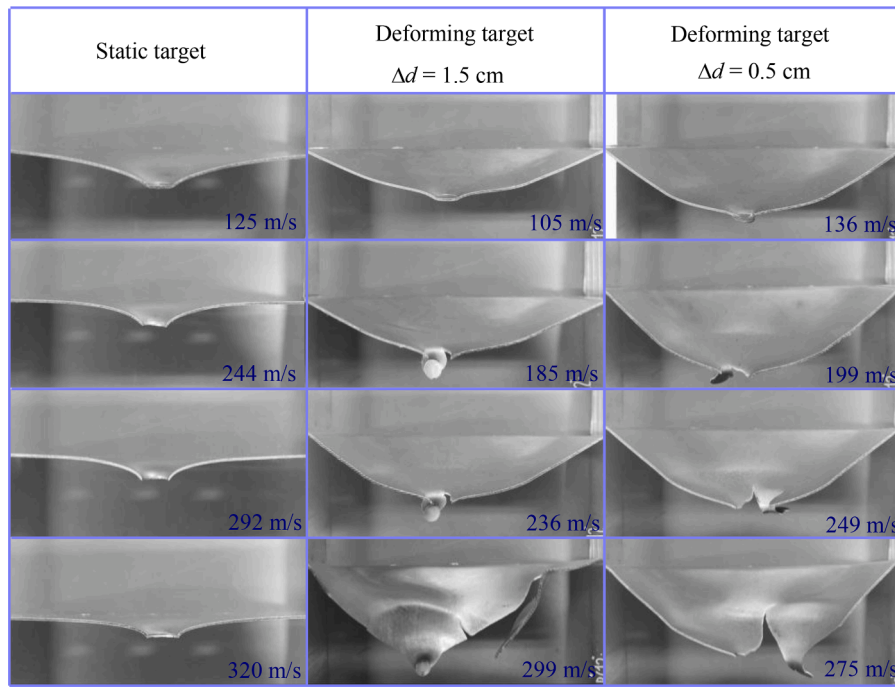


Fig. 4. Cross-sectional views of penetrated thin steel plates under varying impact velocities.

image. For static targets, the plate was perforated by the blunt projectile directly and the perforation mode was plugging dominant, accompanied by hinging. For deforming targets, the final deformation modes include both global deflection and central perforation, the global deflection generated a deforming state of the target in the perforation process. It was observed that the final deflection profiles converted from only deflection to deflection and large petals as the impact velocity increased. The large petals can be explained as that the kinetic energy of the foam sabot was not completely consumed by self-compaction and deflection of the target under high impact velocities, after the deforming target was perforated by the steel projectile, the foam sabot continued to impinge on the target, during which cracks formed around the perforation hole and propagated to the clamped edges, which further formed large petals. Unlike the static targets, where a plug was ‘ejected’ from each target, a stripe of the target was moved out from each deforming target. This incomplete circumferential plug was believed to be induced by unevenness of the target caused by the impact of Al foam sabot. In addition, it was also found that the stripe generated in deforming targets of $\Delta d = 0.5\text{cm}$ was bent backwards, while the stripe generated in deforming targets of $\Delta d = 1.5\text{cm}$ was nearly vertical to target surface. This indicated that the kinetic energy transmitted to the stripe from projectile was also influenced by the deforming extent. In the present study, the phenomenon that deforming affects the ballistic performance and perforation mode of a metallic plate is called “deforming effect”.

3. Cell-based finite element modeling

3.1. Voronoi foam modeling

The technique of 3D Voronoi construction is employed to generate FE models for cylindrical sabots made of close-celled Al foam. The methodology begins with a total of N nuclei randomly placed in a 3D space, where the distance between any two nuclei is larger than a minimum allowable distance, r . Subsequently, based upon the Delaunay triangulation, the space is divided into N closed cells. The boundaries of all the cells constitute the so-called δ -diagram, namely, the Voronoi diagram with an irregularity degree of $\delta = r/r_0$. Here, r_0 is the distance between two adjacent nuclei in a regular tetrakaidecahedral foam model

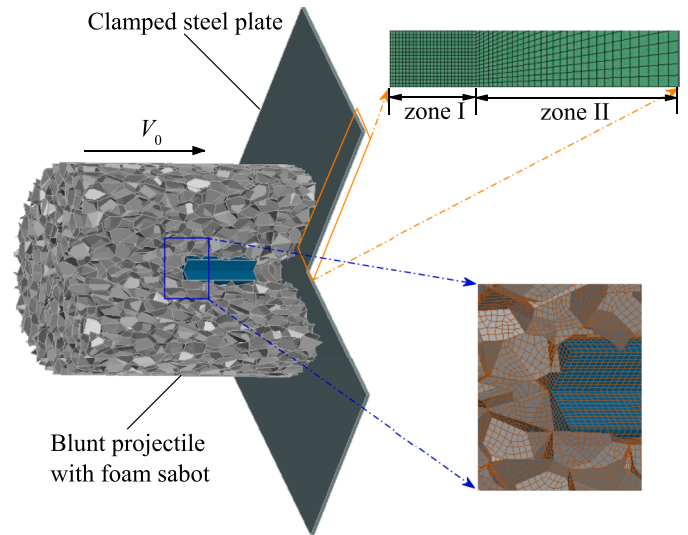


Fig. 5. Finite element model (showing three quarters of model) for thin steel plate impacted by blunt projectile embedded in aluminum foam sabot.

with N cells in volume V , given by:

$$r_0 = \frac{\sqrt{6}}{2} \left(\frac{V}{\sqrt{2}N} \right)^{\frac{1}{3}} \quad (1)$$

With all the cell walls assumed to have a uniform thickness of h , the density of the Voronoi foam is calculated by:

$$\rho_f = \frac{\sum_{i=1}^n A_i \cdot h}{V/m} \cdot \rho_s^f \quad (2)$$

where n and A_i are the number of cell walls and the area of the i th cell wall, respectively, and ρ_s^f denotes the density of cell wall material. By changing the uniform thickness, 3D foam models with different densities can be constructed for FE simulations.

Table 2

Parameters of constitutive model for aluminum.

E_t^f (GPa)	E_t^f (MPa)	σ_{ys}^f (MPa)	ρ_s^f (kg/m ³)	ν
69	58	100	2700	0.3

3.2. Finite element modeling

Ballistic impact on deforming thin steel plate is simulated using full 3D finite element models in Ls-Dyna, as shown in Fig. 5. The Al foam sabot (65 mm in length and 57 mm in diameter; diameter of inner hole 8 mm) is constructed based on the Voronoi foam technique, and meshed with Shell 163 element that has 5 integration points through the thickness of cell walls. Since the foam sabot is mainly used to generate a shock loading, the mesh convergence of foam sabot is checked by comparing the contact pressures between target plate (a fixed rigid target is used) and the Voronoi foam sabot that is meshed with various sizes of shell element (i.e., 0.2 mm, 0.1 mm, 0.05 mm). Since refinement of the mesh size only has slightly influence on the contact pressure, upon considering both mesh convergence and computational efficiency, the size of the shell element is eventually set to 0.2 mm. Both the blunt projectile (20 mm in length and 7.62 mm in diameter) and square steel plate (100 mm in width and 0.9 mm in thickness) are meshed using eight-node brick elements with reduced integration. A global mesh size of 0.5 mm is used for the blunt projectile, while the steel plate is divided into two zones having different mesh sizes so as to improve computational efficiency and maintain numerical accuracy. Zone I has a square edge length of 15 mm in the center, within which the mesh size is 0.3 mm in length. In Zone II, which includes the remaining region of the plate, the mesh size is varied from 0.3 mm to 2 mm. In thickness direction, there are ten elements for both Zone I and Zone II. Mesh sensitivity is carefully carried out for the target plate, both in-plane mesh size and through-thickness mesh size are checked by comparing the maximum central deflection and residual velocity of the blunt projectile, respectively. The results indicate that the above mesh size is sufficient for numerical convergence.

In the present FE simulations, the foam sabot and the blunt projectile impact the edge-clamped steel plate with a common prescribed velocity. An automatic surface to surface contact is set between the blunt projectile and sabot while an automatic node to surface contact is set between the composite projectile (blunt projectile and sabot) and steel plate. Besides, a single surface contact is employed for the sabot. For all contact pairs, a constant coefficient of friction 0.2 is used according to a previous experimental study [38].

For static steel plates, FE models of ballistic impact are also constructed. The models are nearly the same as those for deforming steel plates, except for the lacking of Al foam sabot.

3.3. Material models

The materials involved in FE simulations include the hardened steel (blunt projectile), aluminum (foam sabot), and Q235 steel (target plate). Since the blunt projectile exhibits little deformation during the entire course of impact, as shown in Fig. 7b, the rigid material model is adopted, with a density of 7800 kg/m³ and a Young's modulus of 200 GPa.

For the foam sabot, the material make of its cell walls is characterized with a bi-linear strain-hardening model, given by:

$$\sigma = \begin{cases} E_s^f \varepsilon, & \varepsilon \leq \frac{\sigma_{ys}^f}{E_s^f} \\ \sigma_{ys}^f + E_t^f \left(\varepsilon - \frac{\sigma_{ys}^f}{E_s^f} \right), & \varepsilon > \frac{\sigma_{ys}^f}{E_s^f} \end{cases} \quad (3)$$

where σ_{ys}^f denotes the yielding stress, and E_s^f and E_t^f are the Young's

Table 3

Parameters of constitutive model for Q235 steel [41].

Material property	Value
Density, ρ_s (kg/m ³)	7800
Shear modulus, G (GPa)	75
Static yield strength, A (MPa)	293.8
Strain hardening coefficient, B (MPa)	230.2
Strain rate coefficient, c	0.0652
Thermal softening exponent, m	1
Strain hardening exponent, n	0.578
Reference strain rate, $\dot{\varepsilon}_0$	0.0021
Reference temperature, T_r (K)	293
Melting temperature, T_m (K)	1795
Damage constant, D_1	0.472
Damage constant, D_2	18.728
Damage constant, D_3	-7.805
Damage constant, D_4	-00,193
Damage constant, D_5	3.811

modulus and tangent modulus, respectively. The cell wall material used in the present study is aluminum, with mechanical properties listed in Table 2.

The constitutive behavior of steel is represented by the Johnson-Cook fracture model [39,40], characterized by an equivalent stress defined by:

$$\sigma_{eq} = \left(A + B \varepsilon_{eq}^n \right) \left(1 + \dot{\varepsilon}_{eq}^* \right)^c \left(1 - T^{sm} \right) \quad (4)$$

where σ_{eq} and ε_{eq} denote the equivalent stress and equivalent plastic strain, respectively; $\dot{\varepsilon}_{eq}^*$ is the normalized equivalent plastic strain rate, defined as the ratio of equivalent strain rate ($\dot{\varepsilon}_{eq}$) to a reference strain rate value ($\dot{\varepsilon}_0$); n is the strain hardening parameter; A , B , c and m are material constants. In Eq. (4), the homologous temperature is given as $T^* = (T - T_r) / (T_m - T_r)$, where T is the absolute temperature, T_r is the reference temperature, and T_m is the melting temperature. The fracture strain is given as:

$$\varepsilon_f = \left(D_1 + D_2 \exp(D_3 \sigma^*) \right) \left(1 + \dot{\varepsilon}_{eq}^* \right)^{D_4} \left(1 + D_5 T^* \right) \quad (5)$$

where $D_1 \sim D_5$ are material constants determined from experimental measurements, and σ^* is the stress triaxiality ratio. Fracture occurs when damage of a material element equals unity, and the damage is defined by:

$$D = \sum \frac{\Delta \varepsilon_{eq}}{\varepsilon_f} \quad (6)$$

where $\Delta \varepsilon_{eq}$ is the increment of accumulated plastic strain. In the FE simulations, when the damage in an element reaches its critical value 1, the element is deemed to fail by element erosion. In the present study, relevant material constants are determined from existing tensile test data of Q235 steel [41], as listed in Table 3.

4. Results and analysis

4.1. Validation of finite element model

For both static and deforming steel plates, Fig. 6 compares the numerically calculated ballistic performance (in terms of projectile residual velocity) with that experimentally measured. Good agreement is achieved between experimental data and numerical results, particularly when the impact velocity is larger than the ballistic limit. When the impact velocity is around the ballistic limit, the numerical residual velocities are somewhat higher than those measured. This difference is acceptable since experimental data around ballistic limit always oscillates due to structural response of the target plate.

The experimentally observed and numerically predicted deflection

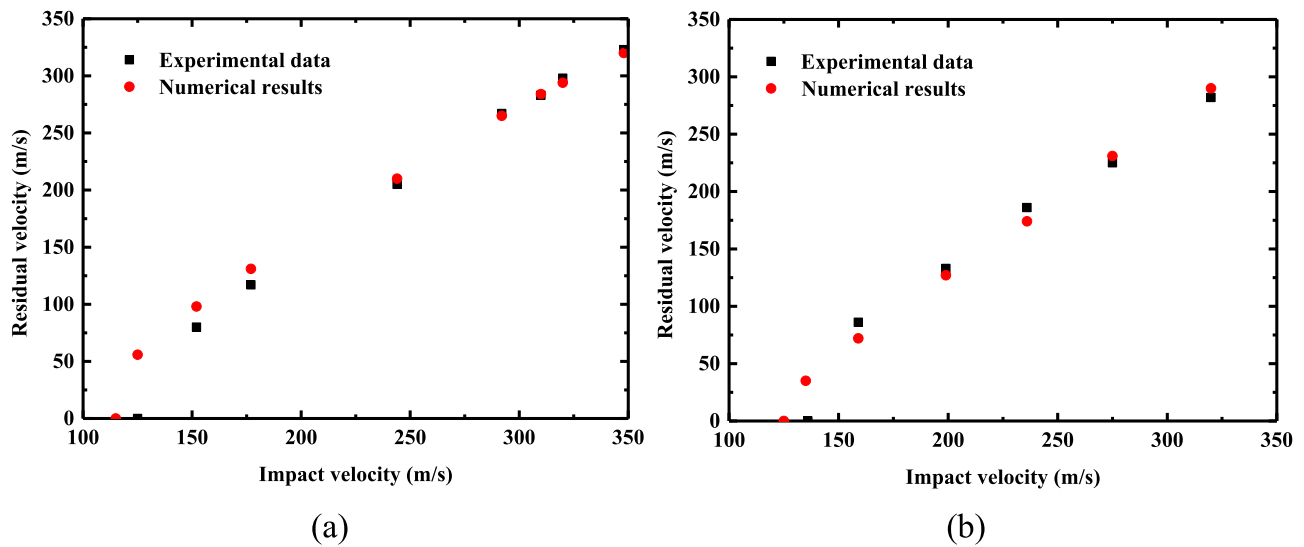


Fig. 6. Comparison between projectile residual velocities obtained numerically and experimentally: (a) static steel plates; (b) deforming steel plates ($\Delta d = 0.5$ cm).

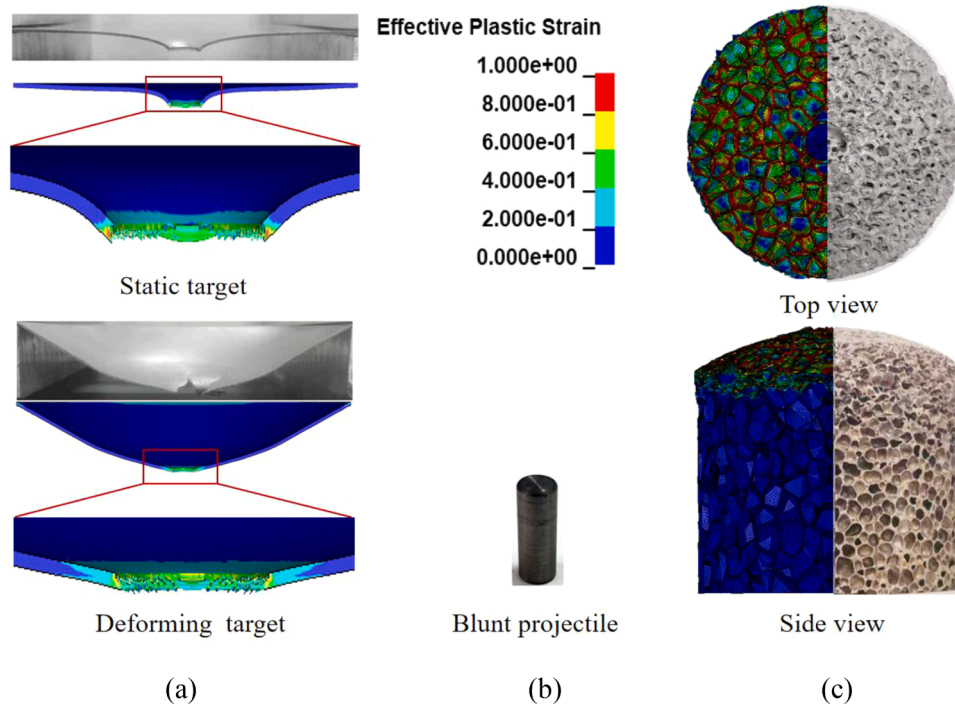
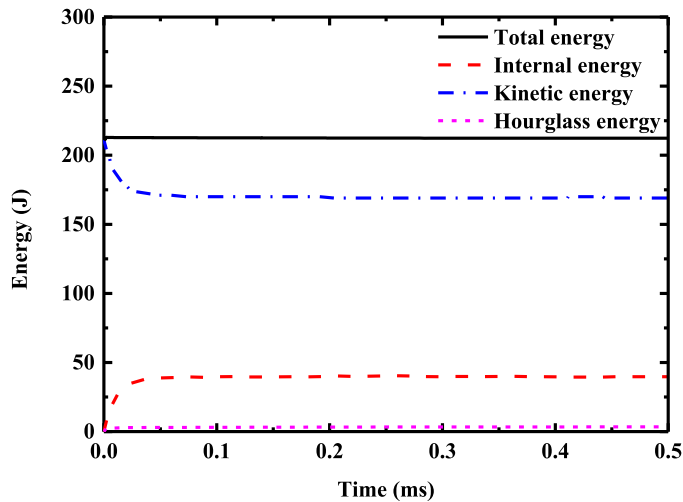


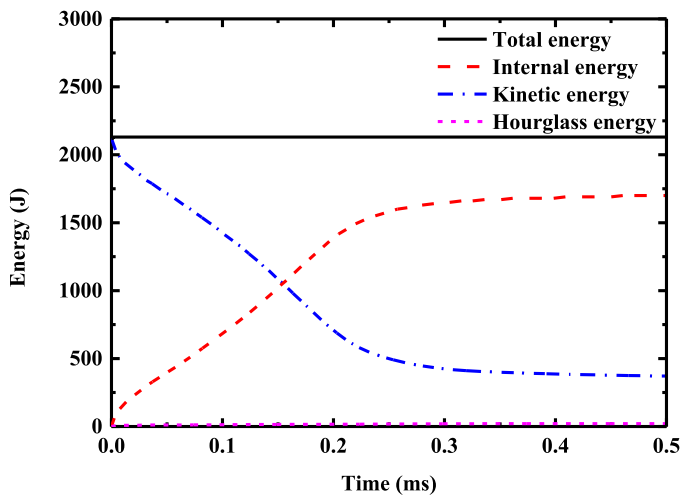
Fig. 7. (a) Comparison between experimentally observed and numerically simulated failure modes of static steel plate impacted by projectile at 244 m/s and deforming steel plate ($\Delta d = 0.5$ cm) impacted by projectile at 249 m/s; (b) Blunt projectile after impact is complete; (c) Comparison between foam sabots employed in experiments and simulations after impact is complete.

profiles and failure (perforation) modes are compared in Fig. 7a for a static plate (impacted at 244 m/s) and a deforming plate (impacted at 249 m/s, $\Delta d = 0.5$ cm), respectively. For both types of steel plate, the experimental and numerical deflection profiles are nearly the same, thus indicating the accuracy of the present FE simulation in capturing the deflection of the plate under foam sabot impact. As for perforation, it is found that the simulated perforation mode of static plate is plugging dominates, which is nearly the same as the experimental result. For the deforming target, the simulated perforation mode is plugging whereas an incomplete circumferential plug perforation mode (cracks and petals) was observed experimentally. The ‘cracks and petals’ mode is referred to be a combined result of initial crack (caused by defects of the target material or unevenness of target induced stress concentration) and

relative lower impact velocity [42,43]. In the present tests, defects of the target material and unevenness of the target (caused by deflection) may exist, which induces the initial crack on the target plate; Besides, the real impact velocity for a deforming target is actually a relative velocity between projectile and moving target (the target gets velocity in the deflection process), which is much smaller than the initial impact velocity of the projectile. These conditions provide a chance for the ‘cracks and petals’ mode to occur. In the simulation, both unevenness of the target and defects of the target material are not exist, thus plugging dominates the perforation mode rather than the ‘cracks and petals’. Comparison between the perforation channels of static target and deforming target indicates that the bulge is obvious in the static target but disappears in the deforming target.



(a)

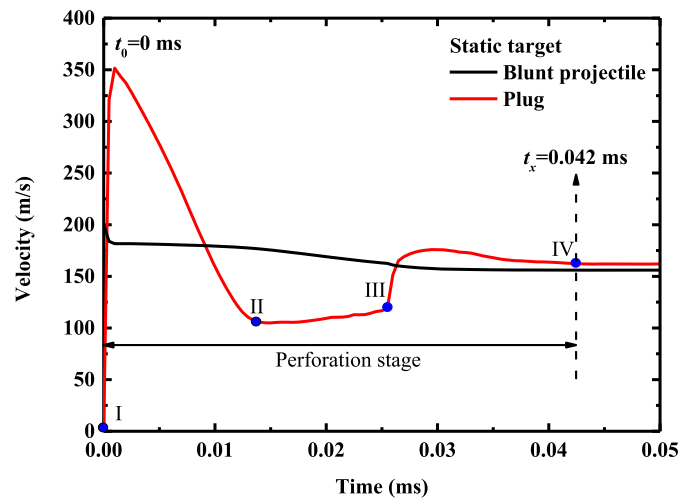


(b)

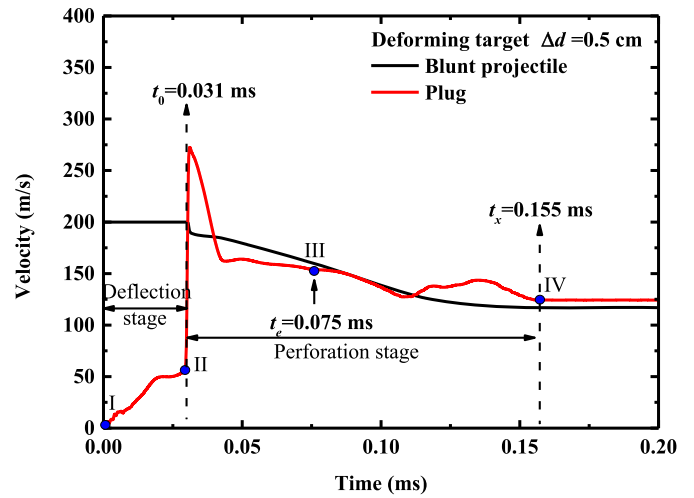
Fig. 8. Energy time history of the impact system: (a) static steel plate; (b) deforming steel plate with $\Delta d = 0.5$ cm.

Fig. 7b presents the profile of the blunt projectile after impact, it is found that the tested projectile is not plastically deformed (projectile mushrooming does not appear), the projectile length is not decreased and the projectile nose diameter is not increased, indicating that the projectile is rigid like. Therefore, using rigid material model to simulate the projectile is viable. Fig. 7c compares further the experimentally observed compression of foam sabot after impact with that numerically simulated. It is seen that both the final length and final nose profile of the simulated foam sabot is similar to the one tested, thus validating the numerical modeling of foam sabot. Therefore, the present FE models are effective in simulating the deflection and perforation of both static and deforming thin steel plates.

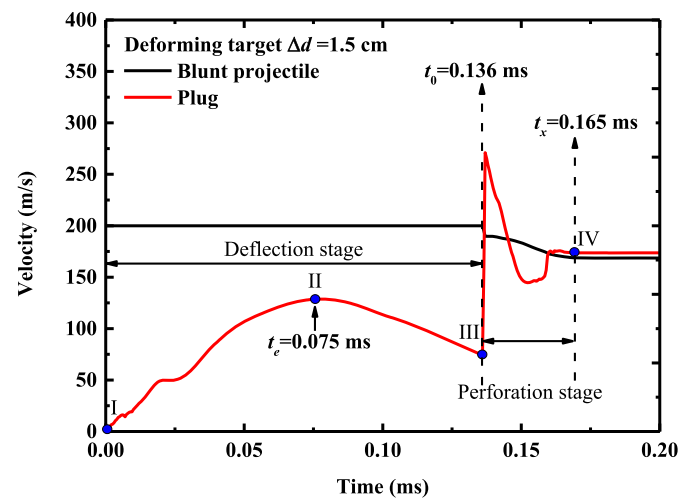
To further check the accuracy and reliability of the numerical models, the energy conservation of the static target (impacted at 244 m/s) and the deforming plate (impacted at 249 m/s, $\Delta d = 0.5$ cm) is investigated, respectively. The energy time histories of the impact system are plotted in Fig. 8. It can be seen that the sum of kinetic energy, internal energy and hourglass energy is equal to the total energy at all time instants. The ratio of the hourglass energy to the total energy is 1.59% and 1.07% for the static target and deforming target,



(a)



(b)



(c)

Fig. 9. Velocity versus impact time histories of blunt projectile and plug for (a) static target, (b) deforming target with $\Delta d = 0.5$ cm, and (c) deforming target with $\Delta d = 1.5$ cm.

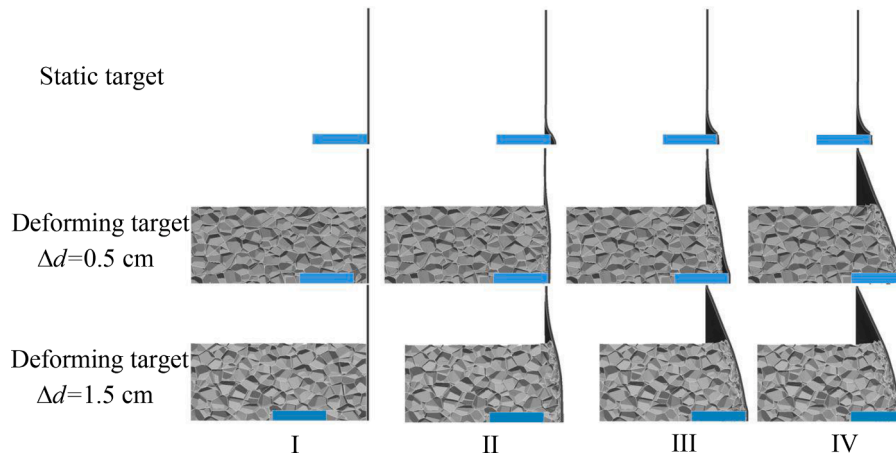


Fig. 10. Comparison between numerically simulated impact processes of static target and deforming targets ($\Delta d = 0.5\text{cm}$ and $\Delta d = 1.5\text{cm}$), the impact velocity is 200 m/s.

respectively, which is less than the threshold 5% typically used to evaluating the accuracy of the numerical calculations [44]. Thus, the impact system energy remains in a reasonable balance during the impact process, indicating that the numerical results are reliable.

4.2. Physical mechanisms underlying the deforming effect

With the impact velocity fixed at 200 m/s, Fig. 9 presents the velocity time histories of both the blunt projectile and plug for both static and deforming targets. It should be noted that the plug is actually the “central part” of the target before it is ejected out, here, we call the “central part” (before ejection) and the plug (after ejection) as “plug” for convenience of expression. The velocity time history of the plug is a combination of these two stages. The deforming target of $\Delta d = 0.5\text{ cm}$ is seen to exhibit a better ballistic performance (i.e., smaller residual velocity) compared with the static target, while the deforming target of $\Delta d = 1.5\text{ cm}$ performs worse (i.e., larger residual velocity). Compared with the static target (Fig. 9a), the dynamic response of both deforming targets (Fig. 9b and Fig. 9c) includes an additional deflection stage, which changes the initial condition of the perforation stage. That is, the initial velocity of the plug (still part of target before being moved out) increases from 0 (static) to 61.5 m/s and 87.3 m/s for the deforming targets of $\Delta d = 0.5\text{ cm}$ and $\Delta d = 1.5\text{ cm}$, respectively, which results in changes of relative velocity between target and projectile. Let t_0 and t_x denote the beginning and ending instant of perforation stage. It is observed that there exists fluctuations for the velocity of the plug in the perforation stage for both static target plate and deforming targets. It is inferred that the fluctuation of the plug (central part) is a result of collisions between the blunt projectile and the plug (central part): the first collision between the projectile and the “central part” leads to a high velocity of the “central part”, then the projectile and the “central part” separates due to velocity difference between them, since the first collision is not enough to move out the “central part” from the target, the “central part” is slowed down due to the pulling force provided by the adjacent region of the “central part”, then the second collision between the blunt projectile and the “central part” happens and the “central part” is finally ejected out. The entire perforation time for the static target is $t_x - t_0 = 0.042\text{ ms}$, while it is 0.124 ms and 0.029 ms for the deforming targets with $\Delta d = 0.5\text{ cm}$ and $\Delta d = 1.5\text{ cm}$, respectively. It is thus inferred that the deflection stage also affects the perforation process. Comparison between the two deforming targets ($\Delta d = 0.5\text{ cm}$ and $\Delta d = 1.5\text{ cm}$) shows that the perforation stage starts at the ascent phase of plug velocity for the deforming target of $\Delta d = 0.5\text{ cm}$, while it starts at the descent phase of plug velocity in the case of $\Delta d = 1.5\text{ cm}$. Besides, it is also found that the difference between the residual velocities of plug and projectile is less than 5 m/s for all the targets tested.

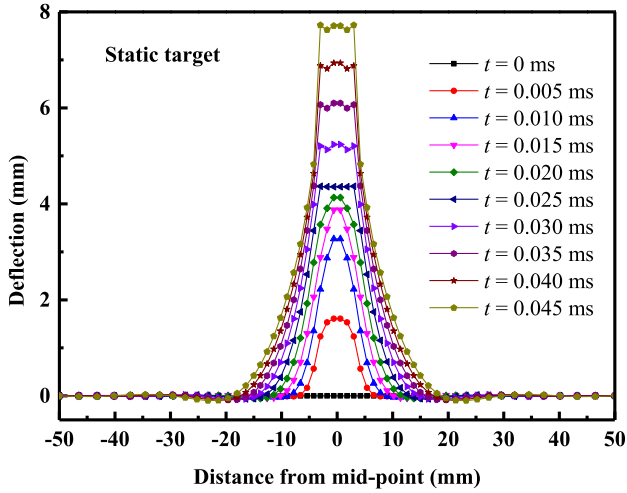
The numerically simulated processes of a blunt projectile penetrating both static and deforming targets are displayed in Fig. 10. It is intuitive that the impact of foam sabot on the target plate makes a deforming target. Time histories of the cross sectional profile of the target is presented for both static target and deforming targets in Fig. 11. It is found that the perforation process for either static or deforming target is plugging dominated, of which the diameter of the plug is nearly the same as the projectile. However, significant dishing (height of the bulge is approximately 4.5 mm) is observed during the perforation process of static target, while dishing (the height of the bulge is hard to distinguish) is not obvious in deforming targets. The dishing is induced by the difference of normal velocities between the “central part” and adjacent region. As the global deflection of the target also provides a normal velocity to the adjacent region, the normal velocity difference between the central plug and adjacent region is decreased, which causes additional flattening of the dishing region for a deforming target, thereto the dishing is not obvious in deforming targets. Fig. 12 presents the time histories of the foam sabot in view of length during the impact process. It is found that the compaction process of the foam sabot is nearly the same for both deforming targets, indicating that nearly equal energy is consumed by the foam sabot in the impact process and nearly equal impulse is transmitted to the deforming targets.

From the view of energy conservation, the energy dissipated during the perforation of a static target comprises the energy E_s consumed by shearing force and the plastic energy E_p consumed by bending and membrane stretching of the dished region. Assume that the plug and projectile attain the same velocity after the latter is moved out (a difference less than 5 m/s is ignored for simplicity). A general expression of energy conservation for static target is thence given by:

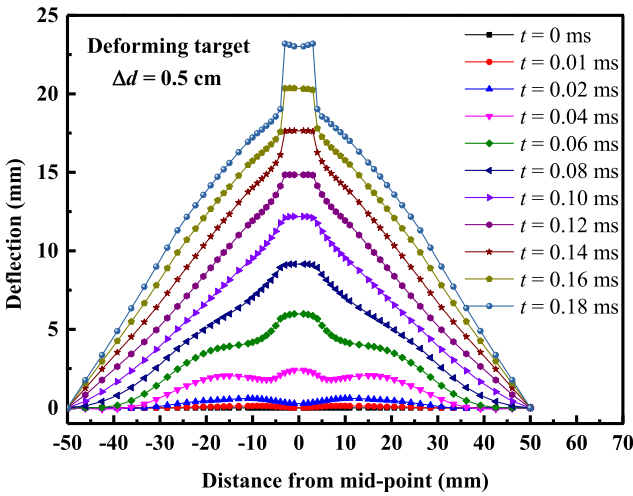
$$\frac{1}{2}m_b V_0^2 = \frac{1}{2}(m_p + m_b) V_f^2 + E_p + E_s \quad (7)$$

where m_b and m_p are the mass of the projectile and plug, respectively, and V_0 and V_f are the impact velocity and residual velocity of the projectile, respectively. It should be noted that wave propagation effects in the acceleration of the plug are ignored as the impact velocity is much lower than the velocity of wave. Besides, the energy consumed by deformation of the projectile is also ignored, since it acts like rigid as observed in the experiments.

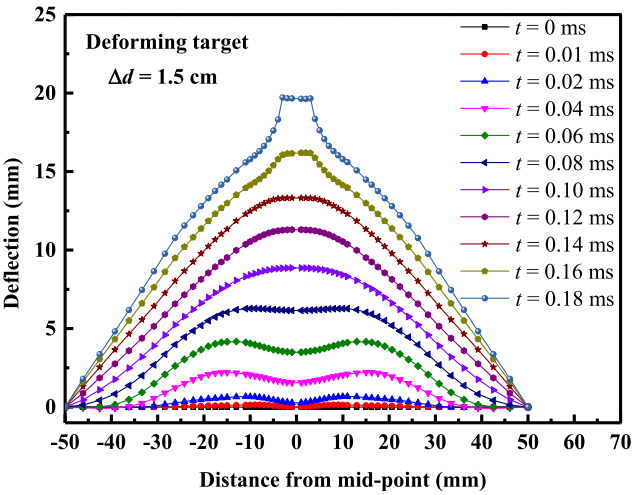
As for the deforming target, the central plug attains a velocity V_i at the end of deflection stage, thus acquiring an initial kinetic energy $m_p V_i^2 / 2$. In the perforation stage, the shear force around the central plug and the bending and membrane stretching of the dished region remain as the two key mechanisms of energy dissipation. However, the dissipated energies E_s and E_p for a deforming target are different from those



(a)



(b)



(c)

Fig. 11. Time-histories of deflection measured from the mid-sections of (a) static target and deforming targets and deforming targets ((b) $\Delta d = 0.5$ cm and (c) $\Delta d = 1.5$ cm), the impact velocity is 200 m/s. (For interpretation of the references to colour in this figure legend, the reader is referred to the web version of this article.)

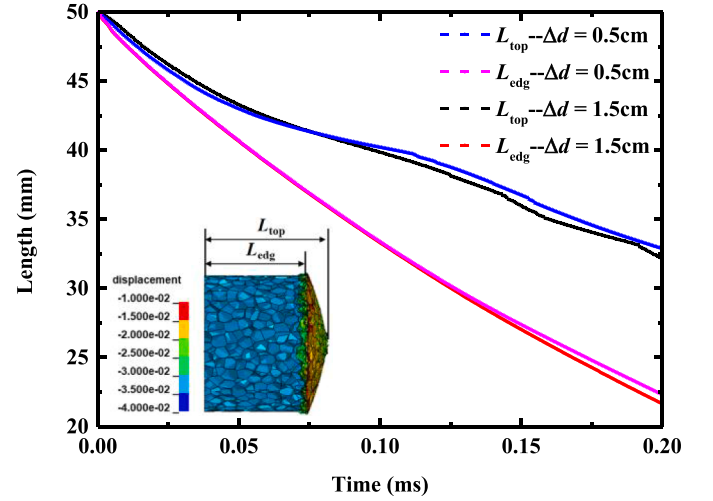


Fig. 12. Time-histories of the foam sabot length for deforming targets ($\Delta d = 0.5$ cm and $\Delta d = 1.5$ cm), the impact velocity is 200 m/s.

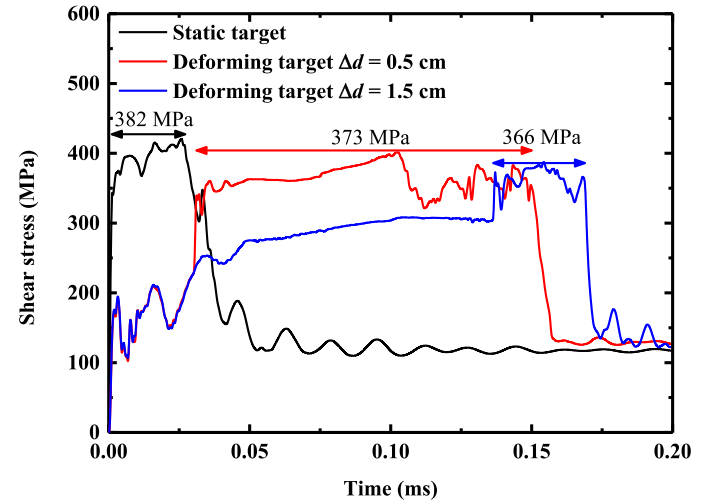


Fig. 13. Numerically calculated shear stress between target and projectile plotted as a function of impact time: comparison between static and deforming targets.

of its static counterpart. Firstly, the extent of plastic deformation in the dished region is different, as observed in Figs. 10 and 11. Secondly, the normal velocity difference between the central plug and adjacent region for a static target is different from that of a deforming target (Fig. 9), thus leading to different dynamic shear forces. It follows that energy conservation for a deforming target can be expressed as:

$$\frac{1}{2}m_b V_0^2 + \frac{1}{2}m_p V_i^2 = \frac{1}{2}(m_p + m_b)V_f^2 + E_p + E_s \quad (8)$$

Comparison between Eq. (7) and Eq. (8) shows that deforming influences the ballistic performance by three items: the initial kinetic energy of the central plug E_k , the dissipated energy E_s , and the dissipated energy E_p . The energy dissipated by shear force is given by:

$$E_s = \pi \tau d_p h \delta_s \quad (9)$$

where τ is the shear stress around the central plug, h and d_p are the thickness of the target and diameter of the plug, respectively, and δ_s is the half-width of shear band, given as:

$$\delta_s = \frac{1 + \sqrt{3}}{8} h \quad (10)$$

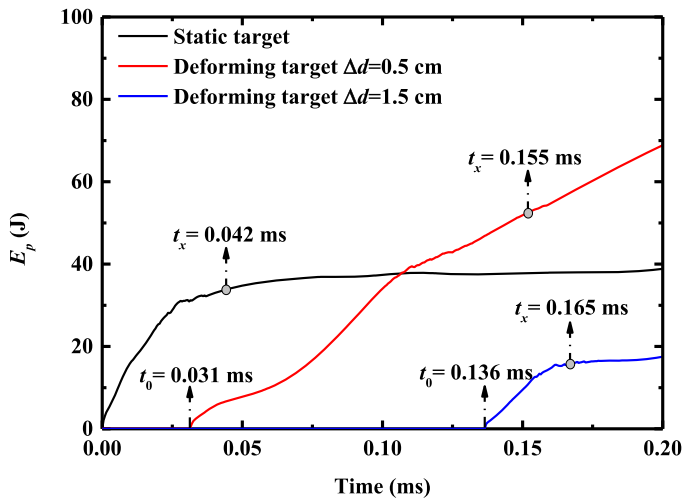


Fig. 14. Energy dissipated by plastic deformation of dished region plotted as a function of time: comparison between static and deforming targets.

According to Fig. 9, the initial velocity of the central plug is 0, 61.5 m/s and 87.3 m/s for the static target, the deforming target of $\Delta d = 0.5$ cm, and the deforming target of $\Delta d = 1.5$ cm, respectively. Correspondingly, the initial kinetic energy E_k is 0, 0.67 J and 1.35 J.

In the FE simulations, E_s is calculated by Eq. (9), in which $\tau = \frac{1}{6} \sum_{i=1}^6 \tau_i$, wherein τ_i denotes the dynamic shear stress of the element in the i th layer through the thickness of a target plate. Fig. 13 presents the average shear stress τ as a function of time for both static and deforming targets. The dynamic shear stress for the static target, the deforming target of $\Delta d = 0.5$ cm, and the deforming target of $\Delta d = 1.5$ cm is calculated to be 382 MPa, 373 MPa and 366 MPa, respectively. The difference between these dynamic shear stresses is caused by difference in normal velocities ($V_0 - V_i$) between the projectile and central plug (just before it is moved out), i.e., the relative velocity is 200 m/s, 138.5 m/s and 112.7 m/s in turn. Larger normal velocity difference leads to higher strain rate, thus leading to larger dynamic shear stress. Upon substituting these FE calculated dynamic shear stresses into Eq. (9), the shear force dissipated energy can be calculated as 3.12 J, 3.04 J and 2.99 J for the static target and deforming targets of $\Delta d = 0.5$ cm and $\Delta d = 1.5$ cm, respectively.

Fig. 14 plots the FE calculated energy E_p as a function of time for both static target and deforming targets, of which E_p is the internal energy of the dished region (i.e., annular region from $r = d_p/2$ to $r = 5d_p$). For a static target, the E_p can be directly obtained. However, for a deforming target, E_p can not be directly obtained, because the internal energy of its dished region includes both perforation induced dishing and global deflection induced flattening. In the present study, the combined deformations of perforation and deflection are decoupled by assuming that E_p of the deforming target is equal to $E_p^c - E_p^f$. Here, E_p^c is the internal energy of the dished region obtained from the target impacted by blunt projectile with foam sabot, while E_p^f is the internal energy of the dished region obtained from the target impacted by foam sabot alone. The results of Fig. 14 demonstrate that the energy consumed by plastic deformation of the dished region is 33.4 J, 53.4 J and 16.7 J for the static

target and deforming targets of $\Delta d = 0.5$ cm and $\Delta d = 1.5$ cm, respectively.

According to the analysis above, most of the energy is dissipated by plastic deformation of the dished region, followed by the shear force; the initial kinetic energy has the least influence. On the basis of static target, the additional energy $\Delta E = \Delta E_k - \Delta E_s - \Delta E_p$ can be calculated as -19.25 J and 18.18 J for the deforming targets of $\Delta d = 0.5$ cm and $\Delta d = 1.5$ cm, respectively, where ΔE_k , ΔE_s and ΔE_p are in turn the difference of E_k , E_s and E_p between a deforming target and a static target. Note that $\Delta E < 0$ means the residual velocity of a deforming target is lower than its static counterpart, and vice versa. Therefore, the deforming target of $\Delta d = 0.5$ cm exhibits a better ballistic performance (smaller residual velocity) than the static target while the deforming target of $\Delta d = 1.5$ cm exhibits worse ballistic performance (larger residual velocity).

Similar analysis is carried out for impact velocities of 150 m/s and 250 m/s. The additional energies between the deforming target and the static target as well as each type of energy (ΔE_k , ΔE_s and ΔE_p) are summarized in Table 4. It is found that ΔE is less than zero for all deforming targets of $\Delta d = 0.5$ cm, but larger than zero for all deforming targets of $\Delta d = 1.5$ cm. From the view of energy conservation, the residual velocities of deforming targets of $\Delta d = 0.5$ cm should be lower than the static targets under impact velocities considered here (150 m/s, 200 m/s and 250 m/s), and vice versa for the deforming targets of $\Delta d = 1.5$ cm. This analysis is in accordance to the experimental results, thus indicating that the foregoing analysis about physical mechanisms underlying the influence of deforming is reasonable. Besides, it is noticed that plastic deformation of the dished region dominates the deforming effect.

4.3. Analysis of influencing factors

Hitherto, it has been demonstrated that the ballistic performance of a deforming target is dependent upon both its deforming state and projectile velocity. Prior to the perforation stage, the deforming state (including deformation extent and velocity of the deforming target) is dependent upon both the impulse pre-imparted to the target and shock resistance of the target. In the experiments, the pre-imparted impulse is determined by the velocity and density of foam sabot as well as the depth of its inner hole, while the shock resistance of the target plate depends on its own thickness. In fact, the pre-imparted impulse is coupled with target deflection, i.e., a target with larger shock resistance exhibits smaller deflection, which then feeds back a larger impulse pre-imparted to the target. To present a general view on how pre-imparted impulse and shock resistance affect separately the ballistic performance of a deforming target, any coupling between the two influencing factors is ignored in subsequent analysis. Further, to characterize the ballistic performance of the deforming target, let the normalized residual velocity and normalized ballistic limit velocity be defined as the residual velocity post-impact normalized by that of static target and the ballistic limit velocity normalized by that of static target, respectively.

4.3.1. Pre-imparted impulse

Prior to the arrival of blunt projectile, the pre-imparted impulse transmitted to a target plate by the front part of foam sabot is dependent upon three factors: inner hole depth Δd , density of foam sabot ρ_f , and impact velocity of foam sabot. To provide a preliminary knowledge about the effect of pre-imparted impulse, the influence of each factor is

Table 4
Additional energies between the deforming target and the static target.

v_i (m/s)	Deforming target ($\Delta d = 0.5$ cm)			ΔE (J)	Deforming target ($\Delta d = 1.5$ cm)			ΔE (J)
	ΔE_k (J)	ΔE_s (J)	ΔE_p (J)		ΔE_k (J)	ΔE_s (J)	ΔE_p (J)	
150	0.89	-0.11	17.2	-16.2	0.31	-0.06	-21.3	21.67
200	0.67	-0.08	20	-19.25	1.35	-0.13	-16.7	18.18
250	0.59	-0.16	26.4	-25.65	2.9	-0.27	-12.6	15.77

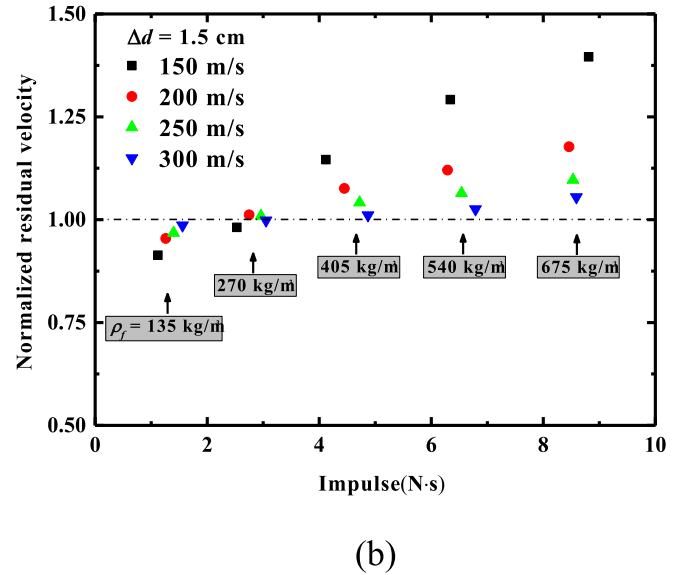
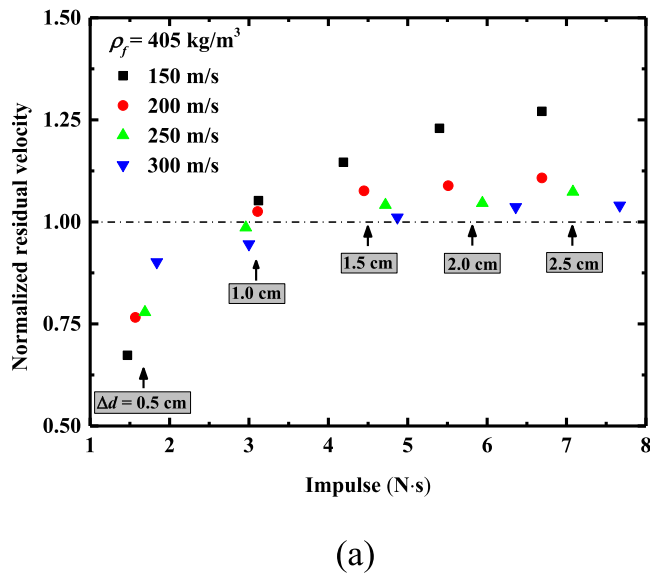


Fig. 15. Normalized residual velocity as a function of pre-impacted impulse: (a) the inner hole depth based impulse and (b) the density based impulse.

investigated individually. The value of pre-impacted impulse prior to the arrival of projectile can be obtained by:

$$I = \int_0^{t_0} f_c(t) dt \quad (11)$$

where $f_c(t)$ is the force transmitted to the target by foam sabot.

Fig. 15a plots the normalized residual velocity as a function of pre-impacted impulse, the latter controlled by varying the inner hole depth Δd while fixing the density of foam sabot at 405 kg/m^3 . The normalized residual velocity post impact increases with increasing pre-impacted impulse for all impact velocities considered, but the increment is gradually reduced. Further, the normalized residual velocity is less than 1 for relatively small pre-impacted impulses, which indicates that the ballistic performance of a deforming target outperforms the static one under these conditions.

Fig. 15b presents the normalized residual velocity as a function of pre-impacted impulse, where the pre-impacted impulse is controlled by varying the density of foam sabot while fixing the inner hole depth at 1.5 cm. The residual velocity increases almost linearly with increasing pre-impacted impulse for all impact velocities. Therefore, the ballistic performance of a deforming plate becomes worse the pre-impacted impulse is increased. Note that Δd and ρ_f actually represent two characteristics of a pre-impacted impulse: duration and amplitude. It is thus concluded that the normalized residual velocity is mainly controlled by the magnitude of the impulse (impact velocity), for the characteristics of pre-impacted impulse affect less. Regardless of the characteristics of pre-impacted impulse, the influence of impact velocity is nearly the same: when the normalized residual velocity is larger than 1, the smaller the impact velocity the larger the normalized residual velocity, causing thus worse ballistic performance of a deforming target relative to its static counterpart; in contrast, when the normalized residual velocity is less than 1, the smaller the impact velocity the smaller the normalized residual velocity, thus better ballistic performance of a deforming target relative to the static one.

4.3.2. Shock resistance of target plate

The shock resistance of a target plate is typically related to the ratio of its thickness to in-plane size h/L , and a larger h/L usually leads to enhanced shock resistance. The effect of h/L on the ballistic resistance of a deforming steel plate can be studied by either varying its thicknesses h or in-plane size L . However, varying h also causes changes in ballistic limit, and hence it is hard to distinguish the effect of shock resistance on

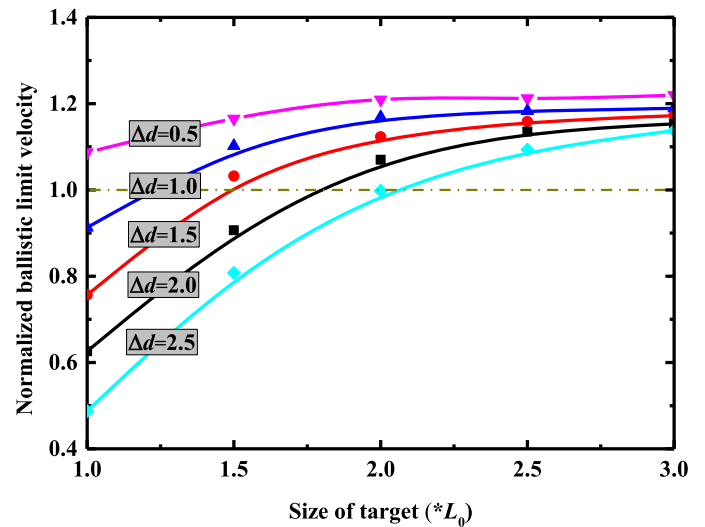


Fig. 16. Normalized ballistic limit velocity of a deforming target with fixed thickness plotted as a function of its in-plane size.

the ballistic resistance of a deforming plate. The effect of h/L is thence studied by varying the in-plane size L from L_0 to $3L_0$, with target thickness h fixed at h_0 .

Fig. 16 plots the normalized ballistic limit velocity of a deforming target (thickness h_0) as a function its in-plane size; different curves refer to different pre-impacted impulses achieved by varying inner-hole depth Δd . The normalized ballistic limit increases with increasing target size for all pre-impacted impulses considered. This indicates that a deforming target with larger shock resistance (larger h/L or smaller L) exhibits inferior normalized ballistic resistance. In other words, the “deforming effect” is less effective in enhancing the ballistic resistance of a target with high shock resistance. Besides, the results reveal that, as the pre-impacted impulse (Δd) is increased, the critical target size above which the ballistic performance of a deforming target outperforms its static counterpart (i.e., the normalized ballistic limit is larger than 1) also increases.

4.3.3. Nose shape of projectile

The nose shape of projectile plays a significant role in the perforation

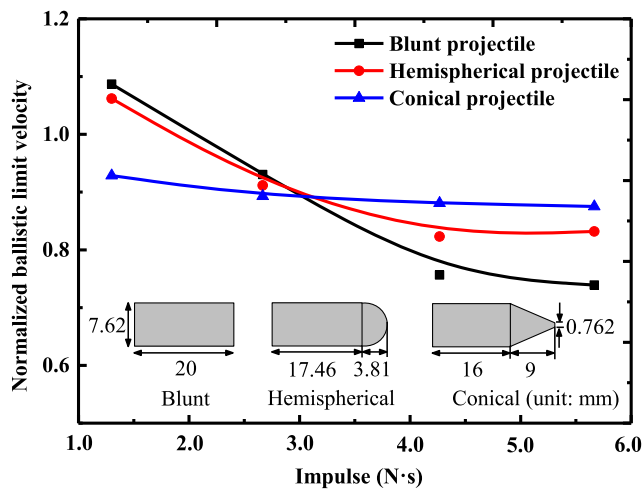


Fig. 17. Normalized ballistic limit velocity of deforming steel plate plotted as a function of impulse (inner-hole depth) for projectiles having different nose shapes.

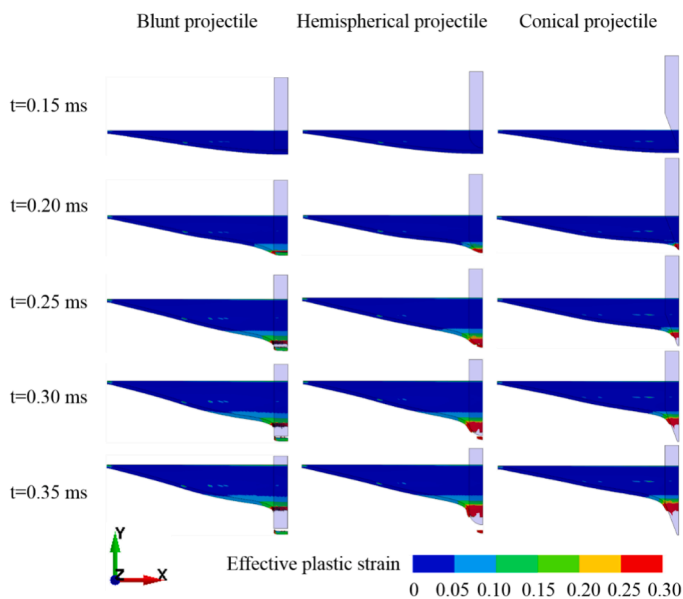


Fig. 18. Simulated perforation of a deforming steel plate (0.9 mm thick) by blunt, hemispherical and conical projectiles having equal mass and equal impact velocity of 200 m/s, respectively.

mode of a target, ultimately affecting the ballistic performance of the latter. The results discussed hitherto are all for blunt nosed projectiles. To quantify the influence of nose shape, in addition to blunt projectiles, hemispherical and conical projectiles are also considered.

Fig. 17 plots the normalized ballistic limit velocity of a deforming steel plate as a function of pre-imparted impulse when subjected to the impact of projectile having varying nose shape. The pre-imparted impulse is again adjusted by varying the inner-hole depth Δd , the projectiles with different nose shapes possess the same mass, and the thickness of target plate remains fixed at 0.9 mm. In Fig. 17, it is seen that the normalized ballistic limit velocity decreases with increasing pre-imparted impulse for blunt both and hemispherical projectiles, although the decrement is more significant in the case of blunt projectiles. In sharp contrast, in the case of conical projectiles, the normalized ballistic limit velocity is not only rather insensitive to the pre-imparted impulse but also less than 1 for all pre-imparted impulses considered. That is, when impacted by conical projectiles, static targets perform better than

deforming targets.

Fig. 18 presents the variation of perforation mode for a deforming steel plate (0.9 mm thick) subjected to impact velocity of 200 m/s as the nose shape of impacting projectile is varied. It is found that the perforation mode of the deforming target varies with projectile nose shape, but is similar to that of its static counterpart: blunt projectile perforates by shear plugging, hemispherical projectile perforates by necking, and conical projectile perforates by forming initially a small hole and then enlargement of the hole. For both shear plugging and necking, the target material in front of the projectile is moved out; for ductile hole enlargement, the target material in front of the projectile is pushed aside. This finding indicates that the deforming of a target plays a role in the case of a plug is formed and then moved out.

5. Anti-penetration design of deforming target

Anti-penetration design of metallic plates is of importance in a variety of engineering and military applications. Traditionally, the anti-penetration design of a target plate is based on ballistic limit data of the target with varying thickness. However, such an approach fails to consider the “deforming effect” on ballistic limit. As have been analyzed above, dependent upon the extent of deforming, a deforming plate may exhibit better or worse anti-penetration performance than a static one, especially when impacted by blunt projectiles. That is, the anti-penetration ability of a deforming plate is not only related to its material make but also to its deforming state. It is therefore necessary to account for “deforming effect” when deforming targets are designed to resist projectiles.

For illustration, a typical design case is investigated to distinguish the difference between static and deforming targets in anti-penetration design. By assuming that a target plate is impacted by a blunt-nosed projectile (velocity fixed at 200 m/s; target material make and blunt projectile same as those described in the previous section), the minimum plate thickness that can resist the projectile impact is determined for both static and deforming plates. Fig. 19a presents the ballistic limit data of static target plates with various thicknesses. It is shown that static steel plates with thickness exceeding 2.25 mm can meet the anti-penetration design requirements. Fig. 19b presents the design chart for deforming target plates, with contour lines denoting different ballistic limit velocities (as labeled on each contour line; unit m/s). The horizontal axis and vertical axis of the figure represent target plate thickness and pre-imparted impulse, respectively. Note that, as previously discussed in Section 4.3, the pre-imparted impulse represents the deforming state of a deforming plate. The design chart reveals that, when the available thickness of target plate is varied from 1.4 mm to 2.5 mm, there exist several combinations of plate thickness and deforming state that can meet specific requirements of anti-penetration design. For instance, if the shock wave pre-imparts an impulse of 3.5 N.s to the target, a plate with thickness larger than 1.73 mm can resist the penetration of projectile. When the pre-imparted impulse is increased to 7.5 N.s, the plate thickness needs to be larger than 2.4 mm to meet the same requirement. If the pre-imparted impulse is not known such that any deforming state is possible, the target plate needs to have a thickness larger than the maximum thickness corresponding to the contour line labeled as ‘200’. Therefore, due to the “deforming effect”, the anti-penetration design of a deforming target plate is more complicated relative to its static counterpart.

6. Conclusions

The ballistic performance of a deforming metallic plate has been systematically investigated using a combined experimental and numerical approach, and compared with its static counterpart. First, experiments are conducted for both static and deforming thin steel plates to characterize their ballistic performance and perforation modes. Then, numerical simulations with the method of finite elements are carried out

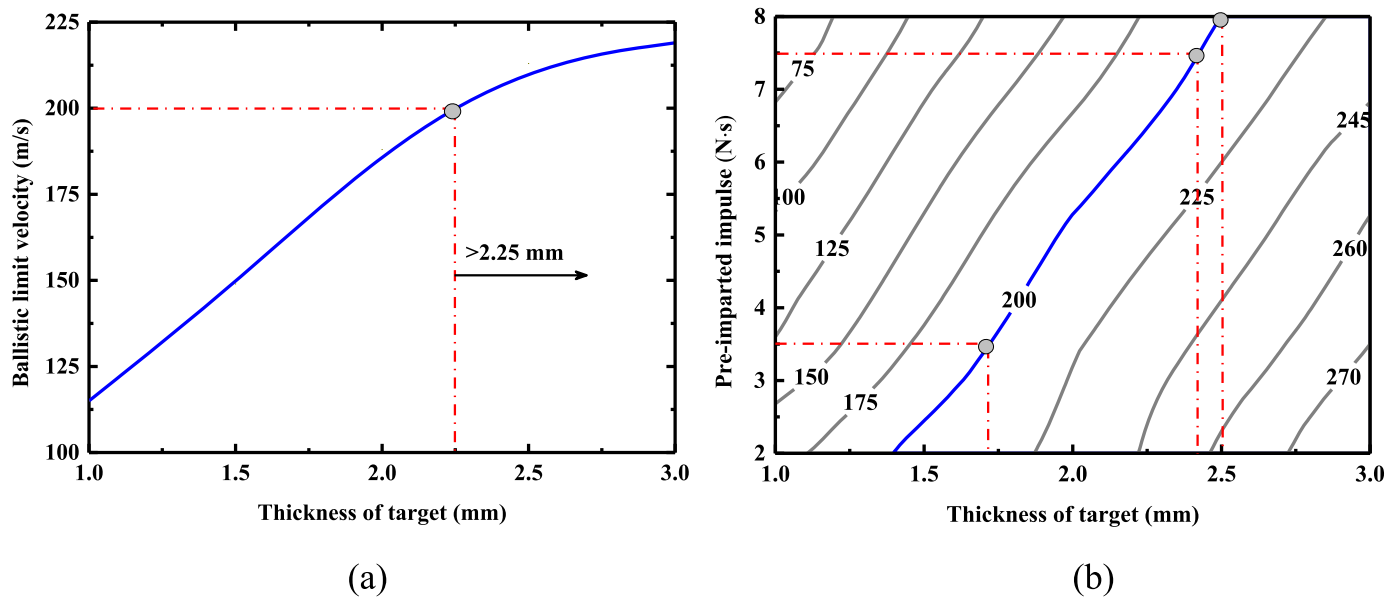


Fig. 19. (a) Ballistic limit velocity plotted as a function of thickness for static target plates, and (b) design chart for deforming target plates.

and validated against experimental measurements. The validated numerical model is subsequently employed to explore physical mechanisms underlying the ballistic performance of a deforming target and quantify the effects of pre-impacted impulse prior to projectile arrival, shock resistance of target material make, and nose shape of projectile. Anti-penetration design of deforming targets is also illustrated. Main conclusions are summarized as follows:

- The ballistic performance and perforation modes of a deforming steel plate are sensitive to its deforming state;
- Deforming induced transmission of kinetic energy to target, energy dissipated via plastic deformation in dished region, and energy dissipated by dynamic shear force during projectile perforation are three major mechanisms underlying the ballistic penetration of a deforming plate;
- While applying a pre-impacted impulse to a target plate before it is impacted by projectile can enhance its ballistic resistance relative to a static target plate, unnecessarily increasing the pre-impacted impulse can also lead to inferior ballistic performance;
- Increasing the inner-hole depth of foam sabot housing the projectile can lead to enlarged critical thickness and in-plane size of target plate above which a deforming plate outperforms its static counterpart;
- The influence of deforming extent on ballistic performance is sensitive in cases when a plug is moved out such as deforming plates subjected to blunt and hemispherical projectiles, but insensitive to conical projectiles since no plug is moved out;
- Deforming effect needs to be accounted for by anti-penetration design of deforming targets.

CRediT authorship contribution statement

Lang Li: Conceptualization, Formal analysis, Writing – original draft. **Qian-Cheng Zhang:** Methodology, Formal analysis. **Tian Jian Lu:** Supervision, Writing – review & editing, Funding acquisition.

Declaration of Competing Interest

The authors declare that they have no known competing financial interests or personal relationships that could have appeared to influence the work reported in this paper.

Data availability

The authors are unable or have chosen not to specify which data has been used.

Acknowledgments

This work was supported by the Fundamental Research Funds for the Central Universities (G2020KY05313), National Natural Science Foundation of China (11902259, 11972185 and 12002156), and Natural Science Foundation of Shaanxi Province (2019JQ-102).

Appendix A: Compressive performance of aluminum foam

Fig. A1 presents the measured quasi-static uniaxial compressive stress versus strain curve of close-celled aluminum foam. The foam is used to construct sabots for blunt projectiles fired via a light-gas gun in the present ballistic impact tests of deforming thin steel plates. Details of foam fabrication and test sample preparation can be found in our earlier study [38]. Under a nominal compressive strain rate of 0.0067 s^{-1} , the aluminum foam displays a plateau strength of approximately 4.5 MPa and a nominal densification strain of 0.7.

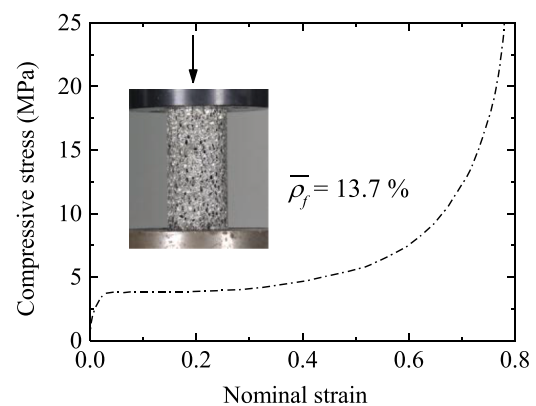


Fig. A1. Experimentally measured quasi-static uniaxial compressive stress versus strain curve of close-celled aluminum foam at a strain rate of 0.0067 s^{-1} .

References

- [1] Recht RF, Ipson TW. Ballistic perforation dynamics. *J Appl Mech* 1963;30(3):384.
- [2] Backman ME, Goldsmith W. The mechanics of penetration of projectiles into targets. *Int J Impact Eng* 1978;16(1):1–99.
- [3] Jones N. Structural impact. Cambridge: Cambridge University Press; 1989.
- [4] Børvik T, Langseth M, Hopperstad OS, Malo KA. Ballistic penetration of steel plates. *Int J Impact Eng* 1999;22(9–10):855–86.
- [5] Arnold JL, Halpern P, Tsai MC, Smithline H. Mass casualty terrorist bombings: a comparison of outcomes by bombing type. *Ann Emerg Med* 2004;43(2):263–73.
- [6] Elsayed NM, Gorbunov NV, Elsayed Mohamed N, Atkins James L. Explosion and blast-related injuries: effects of explosion and blast from military operations and acts of terrorism. Elsevier/Academic Press; 2008.
- [7] Wallace D. Improvised explosive devices and traumatic brain injury: the military experience in Iraq and Afghanistan. *Australas Psychiatry* 2009;17(3):218.
- [8] Børvik T, Langseth M, Hopperstad OS, Malo KA. Perforation of 12mm thick steel plates by 20mm diameter projectiles with flat, hemispherical and conical noses: part I: experimental study. *Int J Impact Eng* 2002;27(1):19–35.
- [9] Iqbal MA, Gupta G, Diwakar A, Gupta NK. Effect of projectile nose shape on the ballistic resistance of ductile targets. *Eur J Mech A-Solid* 2010;29(4):683–94.
- [10] Kpenyigba KM, Jankowiak T, Rusinek A, Pesci R. Influence of projectile shape on dynamic behavior of steel sheet subjected to impact and perforation. *Thin Wall Struct* 2013;65:93–104.
- [11] Kpenyigba KM, Jankowiak T, Rusinek A, Pesci R, Wang B. Effect of projectile nose shape on ballistic resistance of interstitial-free steel sheets. *Int J Impact Eng* 2015;79:83–94.
- [12] Liu D, Stronge WJ. Ballistic limit of metal plates struck by blunt deformable missiles: experiments. *Int J Solids Struct* 2000;37(10):1403–23.
- [13] Singh BB, Sukumar G, Rao PP, Kumar KS, Madhu V, Kumar RA. Superior ballistic performance of high-nitrogen steels against deformable and non-deformable projectiles. *Mater Sci Eng A* 2019;751:115–27.
- [14] Babaei B, Shokrieh MM, Daneshjou K. The ballistic resistance of multi-layered targets impacted by rigid projectiles. *Mater Sci Eng A* 2011;530:208–17.
- [15] Dey S, Børvik T, Teng X, Wierzbicki T, Hopperstad OS. On the ballistic resistance of double-layered steel plates: an experimental and numerical investigation. *Int J Solids Struct* 2007;44(20):6701–23.
- [16] Teng X, Wierzbicki T, Huang M. Ballistic resistance of double-layered armor plates. *Int J Impact Eng* 2008;35(8):870–84.
- [17] Zhou DW, Stronge WJ. Ballistic limit for oblique impact of thin sandwich panels and spaced plates. *Int J Impact Eng* 2008;35(11):1339–54.
- [18] Deng YF, Zhang W, Yang YG, Wei G. The ballistic performance of metal plates subjected to impact by projectiles of different strength. *Mater Des* 2014;54:1056–67.
- [19] Dey S, Børvik T, Hopperstad OS, Leinum JR, Langseth M. The effect of target strength on the perforation of steel plates using three different projectile nose shapes. *Int J Impact Eng* 2004;30(8–9):1005–38.
- [20] GU Bo-hong, Pan XQ. Strain rate effect on the tensile behavior of fibers and its application to ballistic perforation of multi-layered fabrics. *J Donghua University (English Edition)* 2002;1:5–9.
- [21] Børvik T, Hopperstad OS, Langseth M, Malo KA. Effect of target thickness in blunt projectile penetration of Weldox 460 E steel plates. *Int J Impact Eng* 2003;28(4):413–64.
- [22] Palleti H, Gurusamy S, Kumar S, et al. Ballistic impact performance of metallic targets. *Mater Des* 2012;39:253–63.
- [23] Balakrishnan M, Balasubramanian V, Reddy GM. Effect of hardfaced interlayer thickness on ballistic performance of armour steel welds. *Mater Des* 2013;44:59–68.
- [24] Gupta NK, Madhu V. Normal and oblique impact of a kinetic energy projectile on mild steel plates. *Int J Impact Eng* 1992;12(3):333–43.
- [25] Gupta NK, Madhu V. An experimental study of normal and oblique impact of hard-core projectile on single and layered plates. *Int J Impact Eng* 1997;19(5–6):395–414.
- [26] Chen XW, Yang YB, Lu ZH. Perforation of metallic plates struck by a blunt projectile with a nose-cabin-column. *EXPLO SHOCK* 2006;26(4):294–302.
- [27] Chen XW, Yang B, Lu ZH, Chen YZ. Perforation of metallic plates struck by a blunt projectile with a soft nose. *Int J Impact Eng* 2008;35(6):549–58.
- [28] Zhang W, Deng YF, Cao ZS, Wei G. Experimental investigation on the ballistic performance of monolithic and layered metal plates subjected to impact by blunt rigid projectiles. *Int J Impact Eng* 2012;49:115–29.
- [29] Deng YF, Zhang W, Yang YG, Shi LZ, Wei G. Experimental investigation on the ballistic performance of double-layered plates subjected to impact by projectile of high strength. *Int J Impact Eng* 2014;70:38–49.
- [30] Radford DD, Deshpande VS, Fleck NA. The use of metal foam projectiles to simulate shock loading on a structure. *Int J Impact Eng* 2005;31:1152–71.
- [31] Rathbun HJ, Radford DD, Xue Z, He MY, Yang J, Deshpande VS, Fleck NA, Huthinson JW, Zok FW, Evans AG. Performance of metallic honeycomb-core sandwich beams under shock loading. *Int J Solids Struct* 2006;43(6):1746–63.
- [32] Li L, Zhang QC, Zhang R, Wang X, Zhao ZY, He SY, Han B, Lu TJ. A laboratory experimental technique for simulating combined blast and fragment loading. *Int J Impact Eng* 2019;134:103382.
- [33] Tan PJ, Reid SR, Harrigan JJ, Zou Z, Li S. Dynamic compressive strength properties of aluminium foams. Part I-experimental data and observations. *J Mech Phys Solids* 2005;53(10):2174–205.
- [34] Jeon I, Asahina T, Kang KJ, Im S, Lu TJ. Finite element simulation of the plastic collapse of closed-cell aluminum foams with X-ray computed tomography. *Mech Mater* 2010;42(3):227–36.
- [35] Chen YM, Das R, Battley M. Finite element analysis of the compressive and shear responses of structural foams using computed tomography. *Compos Struct* 2017;159:784–99.
- [36] Li L, Xue P, Luo G. A numerical study on deformation mode and strength enhancement of metal foam under dynamic loading. *Mater Des* 2016;110:72–9.
- [37] Li L, Han B, He SY, Zhao ZY, Zhang R, Zhang QC, Lu TJ. Shock loading simulation using density-graded metallic foam projectiles. *Mater Des* 2018:164.
- [38] Jankowiak T, a Rusinek, Lodygowski T. Validation of the Klepaczkoe Malinowski model for friction correction and recommendations on split Hopkinson pressure bar. *Finite Elem Anal Des* 2011;47:191–208.
- [39] Johnson GR, Cook WH. A constitutive model and data for metals subjected to large strains, high strain rates and high temperatures. In: Proceedings of the 7th international symposium on ballistics. 21. *Eng Fract Mech*; 1983. p. 541–8.
- [40] Johnson GR, Cook WH. Fracture characteristics of three metals subjected to various strains, strain rates, temperatures and pressures. *Eng Fract Mech* 1985;21:31–48.
- [41] Guo ZT, Gao B, Guo Z, Zhang W. Dynamic constitutive relation based on J-C model of Q235 steel. *EXPLO SHOCK* (in Chinese) 2018;38:804–10.
- [42] Frontán J, Zhang Y, Ming D. Ballistic performance of nanocrystalline and nanotwinned ultrafine crystal steel. *Acta Mater* 2012;60:1353–67.
- [43] Russell BP. Multi-hit ballistic damage characterisation of 304 stainless steel plates with finite elements. *Mater Des* 2014;58:252–64.
- [44] Li S, Li X, Wang Z, Wu G, Lu G, Zhao L. Finite element analysis of sandwich panels with stepwise graded aluminum honeycomb cores under blast loading. *Compos Part A-APPL S* 2016;80:1–12.